MSWI super heater tube bundle: Particle impaction efficiency and size distribution

Nils Erland L. Haugen [a,*], Steinar Kragset [a,b], Mette Bugge [a], Ragnar Warnecke [c], Martin Weghaus [d]

[a] *SINTEF Energy Research, N-7465 Trondheim, Norway*
[b] *IRIS, N-4068 Stavanger, Norway*
[c] *GKS, Schweinfurt, Germany*
[d] *Weghaus, Waldbüttelbrunn, Germany*

ARTICLE INFO

ABSTRACT

Particle impaction in an in-line super heater tube bundle has been investigated. By using direct numerical simulations for the fluid flow, inertial particles coupled to the fluid through the classical Stokes' drag law have been tracked. Focus has been on the effect of flow velocity, and it is shown that decreasing the flow velocity will drastically decrease the impaction efficiency for some particle radii. Fouling due to the inertial impaction of such particles is consequently very sensitive to the fluid velocity. The results are subsequently combined with particle size distribution measurements from the municipal solid waste incinerator (MSWI) of GKS in Schweinfurt, Germany. Impacting mass fluxes both on the front and back sides of the tubes in the super heater tube bundle are calculated, and it is found that the largest part of the mass impaction stems from particles with diameters in the range from 5×10^{-5} m to 7×10^{-4} m.

© 2012 Elsevier B.V. All rights reserved.

1. Introduction

The deposition of particles on cylinders in an array is an important phenomenon in systems ranging from heat exchangers to fibrous filter screens. The research effort is motivated in the former class of applications by the need to minimize the total particle deposition [1–7], whereas the opposite is true for the filter systems [8–11]. A third motive is to reduce erosion caused by the constant bombardment of solid particles onto the cylinder surfaces in advanced coal-fired combustors and fluidized beds [12–14]. In Strandström et al. [15], a model for the combined effect on deposition and erosion by sticky and non-sticky particles is presented.

Heat exchangers in coal combustion equipments and biomass or waste fired boilers typically consist of cylinders or tubes arranged in bundles around which the flue gas is flowing. To a various extent this gas will always contain fly ash particles resulting from impurities and inorganic material in the fuel. Ash particles in a molten or highly viscous state tend to stick to surfaces on impaction, forming deposits that cause problems in terms of corrosion, efficiency loss and high costs for maintenance. The understanding of the fluid-particle flow and the deposition mechanisms is crucial for the design of such devices [16].

The impaction of particles onto the cylinders strongly depends on the velocity field of the fluid in the vicinity of the surface, as well as on the size distribution of the particles [17–19],

In the recent publication by Weber et al. [19], it was pointed out that it is very difficult to obtain reliable predictions for the particle size distribution by computational fluid dynamics (CFD). They reported further that it is, on the other hand, possible to obtain accurate predictions for the impaction efficiency by means of CFD if care is taken in order to fully resolve the flow field. Consequently this is considered as a crucial step in the development of CFD-based ash deposition models.

In the present study direct numerical simulations (DNS) in the sense that the Navier–Stokes equations have been solved without the use of any kind of modeling, are used in order to accurately resolve the boundary layers around the cylinders. The particle motion is described in the Lagrangian formalism, and the coupling with the fluid is through the Stokes drag. This enables us to study where the deposits will form and how it depends on the Reynolds and Stokes numbers. All the equations have been solved in two dimensions since basically all major flow variations are in the plane normal to the tube axes for low and intermediate Reynolds numbers. The flow is nevertheless considered a three dimensional flow, so that the simulation results can be interpreted as per unit length in the direction of the tube axes. The geometry of interest has been the super heater of the municipal solid waste incinerator (MSWI) of Gemeinschaftskraftwerk Schweinfurt GmbH (GKS) in Germany [20], from which actual measurements of the flue gas particle size distribution are presented towards the end of Section 3.

In the super heater section of a boiler several impaction mechanisms might have an effect. These mechanisms are typically inertial impaction, thermophoresis, turbulent eddy diffusion and Brownian motions. In the current work, all other impaction mechanisms than

---

* Corresponding author.
E-mail address: nils.e.haugen@sintef.no (N.E.L. Haugen).

inertial impaction have been neglected. The reason for doing this is twofold. Firstly inertial impaction is the most important impaction mechanism at least for large particles [4,19], and secondly inertial impaction is also the most general mechanism; by performing a very fundamental study on this mechanism separately, it will be possible to clearly distinguish the importance of the different mechanisms at a later stage. A general investigation with all the impaction mechanisms included, but under several assumptions and approximations, has been made at GKS with a commercial CFD program [21]. In the present study, the effect of inertial impaction alone in a super heater tube bundle is assessed by combining simulation results for the impaction efficiency with the measured particle size distribution of the MSWI of GKS in Schweinfurt.

This study is an extension of previous work by Haugen and Kragset [17] where the particle impaction on a single cylinder was investigated.

2. Equations

The simulations are carried out using THE PENCIL-CODE [22], where the governing fluid equations are

$$\rho \frac{Du}{Dt} = -\nabla P + \nabla \cdot (2\mu S) \tag{1}$$

and

$$\frac{D\rho}{Dt} = -\rho \nabla \cdot u, \tag{2}$$

where t is time, P is pressure, u is velocity, $\mu = \rho \nu$ is the dynamic viscosity, ν is the kinematic viscosity and ρ is density.

$$\frac{D}{Dt} = \frac{\partial}{\partial t} + u \cdot \nabla \tag{3}$$

is the advective derivative and the rate of strain tensor is

$$S = \frac{1}{2} \left(\nabla u + (\nabla u)^T \right) - \frac{1}{3} \nabla \cdot u. \tag{4}$$

The isothermal equation of state,

$$P = c^2 \rho, \tag{5}$$

is used, where c is the speed of sound. The set of Eqs. (1) and (2) is solved at every grid point for every time step. As is seen in the above equations no models or filters are used. As a consequence all spatial and temporal scales must be resolved by the simulation. This requirement has led to the use of a very high resolution grid of 1024×4096 grid points in two dimensions in order to resolve a domain of 0.2 m × 0.8 m. Since no filters are used, and the discretization scheme is of high order, all the small scale kinetic energy is, as in nature, dissipated purely by the molecular viscosity.

While the fluid equations are solved at predefined grid points, the particles are tracked individually. The particle velocity is evolved in time by

$$\frac{dv}{dt} = \frac{F_D}{m_p}, \tag{6}$$

while the particle position behaves as

$$\frac{dx}{dt} = v, \tag{7}$$

where m_p, v and x are the mass, velocity and position of the particle, respectively. The force F_D is the drag force,

$$F_D = \frac{m_p}{\tau_p} (u - v). \tag{8}$$

No other forces are included in this work. The particle response time is

$$\tau_p = \frac{Sd^2 C_c}{18\nu(1 + f_c)}, \tag{9}$$

where $f_c = 0.15 \text{Re}_p^{0.687}$ is negligible for small particles and $S = \rho_p/\rho$. The particle Reynolds number is $\text{Re}_p = (d|v - u|)/\nu$, the particle diameter is $d = 2r$ when r is the particle radius,

$$C_c = 1 + \frac{2\lambda}{d} \left(1.257 + 0.4e^{-(1.1d/2\lambda)} \right) \tag{10}$$

is the Stokes–Cunningham factor, and λ is the mean free path for a typical molecule in the gas.

Here ρ_p is the density of the particle. Assuming all particles to be small enough in order to neglect f_c and at the same time much larger than the mean free path of a molecule yields

$$\tau_p = \frac{Sd^2}{18\nu} \tag{11}$$

which is a unique number for a particular particle size in a given flow. For a more detailed description of the simulations and THE PENCIL-CODE see Haugen and Kragset [17].

3. Results

The super heater of the MSWI in the GKS plant [20] consists of a non-staggered tube bundle where the centers of the tubes are separated by 200 mm in the transverse direction and by 100 mm in the streamvise direction, see Fig. 1. Each tube has an outer diameter of 33.7 mm and the mean velocity and temperature of the fluid approaching the super heater are 5 m/s and 600 °C, respectively. This leads to a Reynolds number based on the mean velocity and the cylinder diameter of 1685 since a flue gas of 600 °C yields a kinematic viscosity of approximately $10^{-4} \text{m}^2/\text{s}$. In all of the following we have set the particle–fluid density ratio to $S = 1000$.

The simulations presented here use periodic boundaries in the transverse direction; this means that simulating a single tube row would represent an infinite number of tube rows. This is due to the fact that for periodic boundary conditions what goes out on one side is immediately inserted on the other side of the domain. In the streamvise direction the five first tubes are simulated. Five tubes are chosen because initial calculations showed that the conditions after tube number five are essentially the same as after a tube much further downstream.

3.1. Impaction efficiency as a function of Stokes number

The main focus in the current work is the impaction efficiency $\eta = N_{\text{impact}}/N$ as a function of the Stokes and Reynolds numbers. N is here defined as the number of particles whose centers of mass initially are moving in the direction of the tube bundle and N_{impact} is the number of particles impacting on the tube. Since eddies can deflect particles substantially, particles that initially were not moving in the direction of the tube bundle may nevertheless impact, causing η to potentially exceed unity. An impaction efficiency larger than one will in certain cases result also if there is only a single target tube because of the particles' finite extents [17]: Whenever a particle whose center of mass moves closer to the tube than one particle
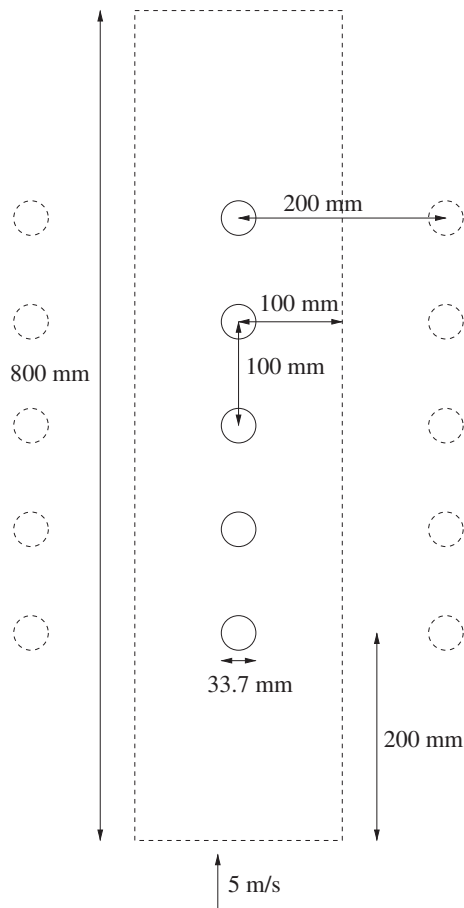
Fig. 1. Here the geometry of the first five tubes of the GKS plant is shown. The dashed rectangle corresponds to the domain of the simulations, where the lower boundary is the inlet and the upper boundary is the outlet. The side boundaries are periodic, mimicking an infinite number of tube rows on each side of the domain as illustrated by the two dashed tube rows on each side of the rectangle.

radius, it is included into N_{impact}. In N however, all particles are regarded as point-like objects, and $N_{\text{impact}} > N$ is consequently possible.

On impact the particle is removed from the simulation. Alternatively, a rebounding of the particles could have been allowed, but to which degree this should happen would require knowledge of material specific parameters such as the sticking coefficient [4]. A total removal of the particles is therefore conveniently used, although the opposite extremum could equally well have been chosen, depending on the application of interest. Furthermore the Stokes number is given by

$$\text{St} = \frac{\tau_p}{\tau_f} \tag{12}$$

and the Reynolds number

$$\text{Re} = \frac{uD}{\nu}, \tag{13}$$

where

$$\tau_f = \frac{D}{2u} \tag{14}$$

is the fluid relaxation time and D is tube diameter.

In the upper row of Fig. 2 the impaction efficiency on the front side of the tubes is shown as a function of Stokes number. For the low Reynolds number simulation it is seen that the only tube that experiences impaction is the first one. This is reasonable as a Reynolds number of only 20 is sub-critical to the existence of von Karman eddies, and consequently there is no fluid motion trying to force the particles towards the other cylinders as soon as they have passed the first one. Such a low Reynolds number is however not very relevant for a boiler as the heat transfer rate from the fluid to the tubes downstream of the first tube would have been very low since the hot flow passes between the tube rows without interacting with the tubes.

As the Reynolds number is increased to 421 (central upper plot in Fig. 2) the presence of von Karman eddies leads to particles impacting also on the tubes downstream of the first tube. Studying the individual cylinders it can be seen that except for the initial cylinder, which has an impaction efficiency which is monotonically increasing with increasing Stokes number, all the downstream cylinders have peak impaction efficiencies in the Stokes number range of 0.7 to 2. The reason for this is that the particles with very large Stokes numbers are not as efficiently affected by the von Karman eddies, and consequently move straight on as they have passed the first tube. The particles with very small Stokes numbers do not impact on the downstream tubes simply because they follow the flow too well. The remaining are the intermediately sized particles, having the largest impaction efficiency as they are indeed affected by the von Karman eddies, but they are still large enough in order to penetrate the boundary layer around the tubes.

Increasing even further the Reynolds number to 1685 the impaction efficiency of the downstream tubes is increased even more. The major reason is the decrease in the boundary layer thickness as the Reynolds number is increased. The boundary layer is effectively working as a shield for the tubes against particle impaction. Another reason of the increased impaction efficiency is the increased intensity in the eddies generated by the cylinders. This is clearly seen in Table 1 where the rms and maximum values of the transversal velocities are shown. As expected the transversal velocities increase with Reynolds number, and the maximum velocity is even larger than the mean flow velocity for the largest Reynolds numbers. This is reflected in the observation that for Re = 1685 cylinders numbers 2, 4 and 5 all have larger impaction efficiency than the first cylinder for Stokes numbers smaller than 0.3.

Focusing now on the back side impaction it is seen in the lower left plot of Fig. 2 that there is no back side impaction for Re = 20, this is again reasonable because there are no von Karman eddies generated for this Reynolds number and hence that there is no effect which can force the particles to move towards the back side of the cylinders.

For Re = 421 (central lower plot of Fig. 2) it is seen that back side impaction occurs for all cylinders except for the first one. The impaction efficiency is however relatively small, and it is largest around St = 4. In particular it is worth mentioning that the relatively large back side impaction for cylinder 3 around St = 4 is due to a very prominent particle stagnation between cylinders 3 and 4. Particles tend to stay in this stagnation point for long times, but as they leave they gain velocity opposite to the mean flow velocity in the direction of cylinder 3. As particles with St = 4 are large particles they do not have any problems penetrating the boundary layer on the back side of cylinder 3.

As the Reynolds number is increased to Re = 1685 (lower right plot of Fig. 2) the overall back side impaction shows a bimodal behavior. For the first cylinder we recover the same results as seen on a single cylinder in Haugen and Kragset [17]; that there is back side impaction only for Stokes numbers smaller than ~0.1. The peak in impaction efficiencies at the smallest Stokes numbers is due to the second cylinder, while the large Stokes number peak is due to the last cylinder. It should be noted that the cause of the two peaks is
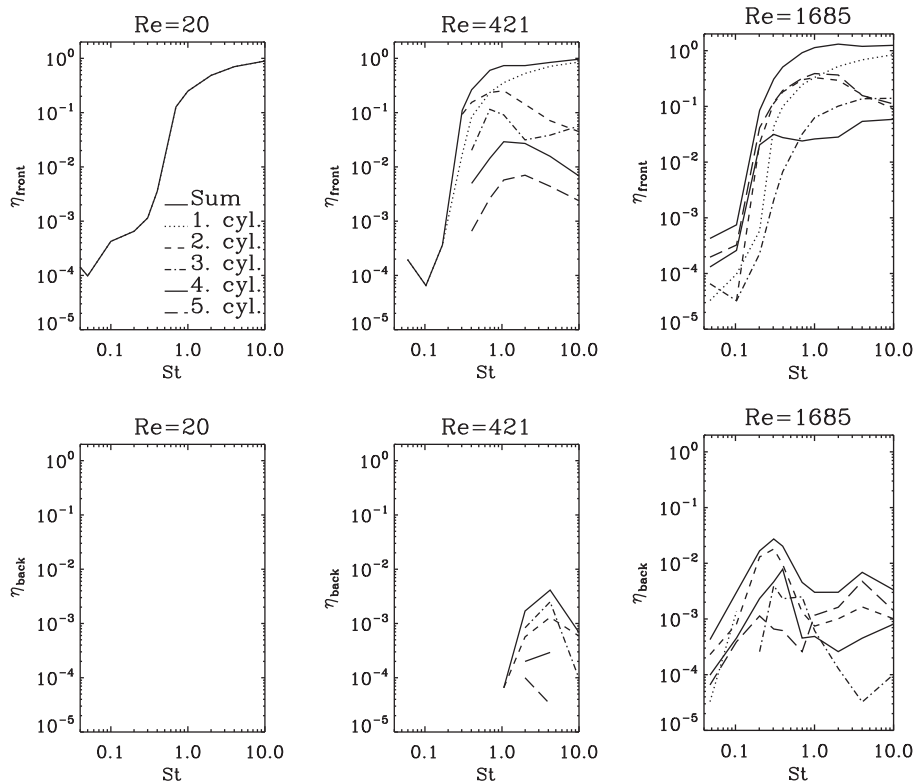
Fig. 2. Front side (upper plots) and back side (lower plots) impaction efficiency as a function of Stokes number for different Reynolds numbers. Here both the impaction efficiencies for the sum of all the five tubes (solid line) and for each individual tube are shown.

fundamentally different. The peak at small Stokes numbers is caused by particles being captured in the eddies behind a given cylinder and are then given a velocity in the direction of the back side of the cylinder by this eddy. This is the same mode of back side impaction as also found for a single cylinder [17], and it leads to impaction essentially on all angles on the back side. The second peak is caused by particles being diverted by eddies formed by cylinders further up-stream in a neighboring tube row. These particles will then approach the cylinder not from the front side but rather from the side, which then allows for particle impaction at an angle slightly larger than 90°. It is indeed found that for Stokes numbers larger than unity almost all the impaction on the back side occurs at angles between 90° and 110°.

In Fig. 3 it is shown that the larger the Reynolds number the larger is both the total front and total back side impaction efficiency. Here total refers to the sum of the impaction efficiencies for all cylinders (which is indeed the same as the solid lines in Fig. 2). In Haugen and Kragset [17] it was shown that this was also the case for the front side impaction on a single cylinder for Stokes numbers larger than ~0.2. For smaller Stokes numbers, however, Haugen and Kragset [17] found that the impaction efficiency was largest for the small Reynolds numbers. Here the same trend is seen between Reynolds

numbers of 20 and 421, but with a Reynolds number of 1685 the impaction efficiency is always larger than for the smaller Reynolds numbers. Regarding the back side impaction Haugen and Kragset [17] found that for a single cylinder there was no back side impaction for Stokes numbers larger than 0.13. This is clearly not the case here.

3.2. Impaction efficiency as a function of particle diameter

From the practical point of view, in an industrial boiler, it might be more interesting to predict the impaction efficiency as a function of the particle size than of the Stokes number. The latter is dependent on the super heater geometry and dimensions, whereas more or less the same particle size distribution will be emitted from the furnace no matter what is done with the super heater section.

Table 1
Root-mean-square and maximum transversal velocities for different Reynolds numbers.

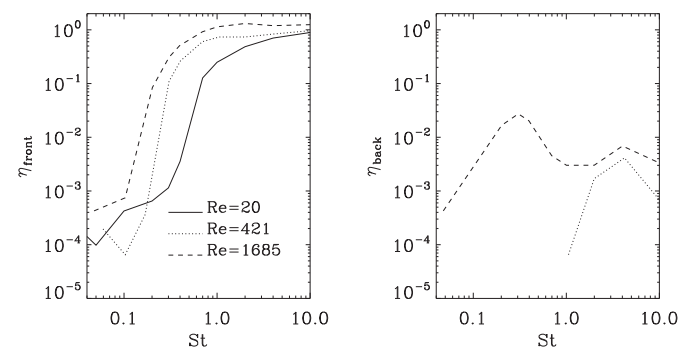| Re	$u_{trans,rms}$	$u_{trans,max}$
–	m/s	m/s
20	0.3	2.9
421	1.2	8.1
1685	1.6	11.3

Fig. 3. Front side (left plot) and back side (right plot) impaction efficiency for different Reynolds numbers as a function of the Stokes number.

The Stokes number can be expressed as a function of the Reynolds number by

$$\text{St} = \frac{d^2 S u}{9 \nu D} = \frac{d^2 S}{9 D^2} \text{Re} \tag{15}$$

which shows that, if the Reynolds number is decreased by either decreasing the velocity or increasing the viscosity, the Stokes number is also decreased. Consequently it is seen that the Stokes number varies linearly with the Reynolds number, such that a given particle size corresponds to a smaller Stokes number when the Reynolds number is small. From Fig. 2 it is seen that the total front side impaction efficiency is monotonically decreasing with decreasing Stokes number. This means that for a given particle size the front side impaction efficiency will always decrease with the Reynolds number. This is shown more clearly in Fig. 4 where the total front and back side impaction efficiency is shown as a function of particle size for the three different Reynolds numbers. It is seen that when impaction efficiency is plotted as a function of particle size the difference between small and large Reynolds numbers is even more prominent than when plotted against Stokes number. As an example the capture efficiency of a particle with diameter of 60 μm is around 10^{-4} for Re = 421 while it is around 0.7 for Re = 1685, which is a difference by a factor of more than three orders of magnitude.

In this work the Reynolds number is changed by changing the viscosity, this is however equivalent to inversely changing the velocity.

3.3. Particle size distribution

The particle impaction efficiency has been combined with measurements of the flue gas particle size distribution in the super heater of the MSWI in Schweinfurt, Germany, in order to provide quantitative predictions for mass impaction on an actual tube bundle. In this subsection only the previously mentioned simulations with a Reynolds number of 1685 have been used.

In the measurements, the mass density $\hat{\rho}_p$ of particles in the flue gas is size fractionated using different techniques for coarse ($d \gtrsim 20\,\mu m$) and fine ($d \lesssim 20\,\mu m$) particles. For details, see [23]. Note that this density is different from the internal particle density ρ_p and is defined as the mass of the particles (of a given size) per fluid volume in which they are contained. The results for different ranges of particle sizes have accordingly been split into bins. That is, in particle bin i the mean density $\hat{\rho}_{p,i}$ of particles with diameters in the range between d_i and d_{i+1} is given (see Table 2).

As the time-step of the numerical simulations scales as ~d^2 for small particle diameters it is obvious that it is not practically feasible to run simulations with extremely small particle diameters. It was
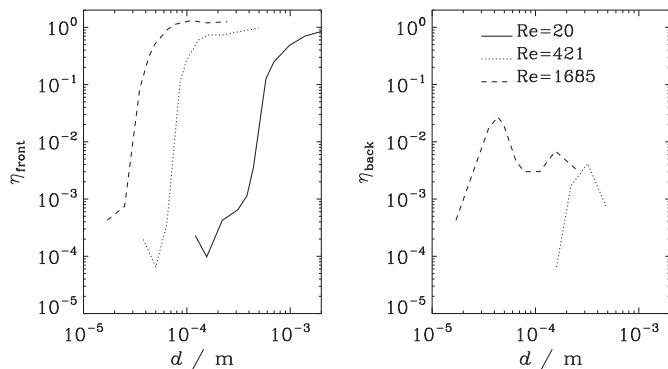
Table 2
Particle size distribution just before the super heater of the MSWI in Schweinfurt, Germany.

d μm	d_{min} μm	d_{max} μm	$\hat{\rho}_{p,i}$ g/m³	ϕ_i g/(s m²)	η_{front}	$\dot{m}_i$ g/(s m²)
2.84	2.29	3.52	0.006	790	0.0008	0.66
4.37	3.52	5.63	0.003	263	0.0007	0.20
7.23	5.63	8.98	0.002	92	0.0006	0.05
12.0	8.98	16	0.004	65	0.0003	0.02
40	25	63	0.023	91	0.2247	21
89	63	125	0.120	315	1.1967	377
177	125	250	0.220	296	1.2082	358
354	250	500	0.270	179	1.0105	181
707	500	1000	0.078	26	1.0209	27
1400	1000	2000	0.046	7	1.0415	8

found that particle sizes less than a couple of micrometers would require too much computer time. There are, however, experimental results available for $\hat{\rho}_p$ down to 0.041 μm, but they have been omitted due to the restrictions introduced by the simulations.

The average particle diameter[1] d_i of the interval $(d_{i,min}, d_{i,max})$ will from now on be used as the representative diameter.

In the upper plot of Fig. 5 the mean mass density is shown for particles in the range 3×10^{-6} m to 1.4×10^{-3} m. Upstream of the first tube, the mean mass flux rate per tube length of particles in bin i flowing in the direction of the tubes is

$$\Phi_i = \hat{\rho}_{p,i} D u, \tag{16}$$

and the corresponding specific mass flux rate for a particle diameter within the bin is then

$$\phi_i \equiv \frac{\Phi_i}{\Delta d_i} = \frac{\hat{\rho}_{p,i} D u}{\Delta d_i}, \tag{17}$$

where $\Delta d_i = d_{i+1} - d_i$. In the following all fluxes are measured per tube length.

The specific rate of mass impacting on the front side of the tubes in the tube bundle due to particles with diameters belonging to bin i is found as

$$\dot{m}_i = \phi_i \eta_{front}(d_i), \tag{18}$$

and the results are shown in the lower plot of Fig. 5. In the central plot of Fig.5 the front side impaction efficiency is shown. This is essentially the same plot as the dashed line in Fig. 4, but with a slightly extended range towards smaller particles.

Integrating $\dot{m}$ over particle diameter yields the total mass captured per time unit. In Fig. 6 $\dot{m}$ is consequently shown in a linear fashion such that the area under the graph corresponds to the total mass impaction rate. From this it is seen that the major part of the mass deposition from particle impaction is due to particles in the range from 5×10^{-5} m to 7×10^{-4} m. So even though the impaction efficiency of all particles with $d > 7 \times 10^{-4}$ m is essentially unity, or even in excess of unity, the total impacted mass due to these particles is not very large because of their low abundance in the flow.

The specific rate of mass impacting on the *back* side of the tubes, $\dot{m}_{back}$, is shown in Fig. 7. It is seen that the specific rate of back side mass impaction is first of all much smaller than what is found on the front side. Furthermore the main peak of $\dot{m}_{back}$ is shifted slightly towards smaller particles compared to its front side counterpart.

Fig. 4. Front side (left plot) and back side (right plot) impaction efficiency for different Reynolds numbers as a function of the particle diameter.

---

[1] The average diameter is not an arithmetic mean but is based on a fundamental knowledge of the measurements.
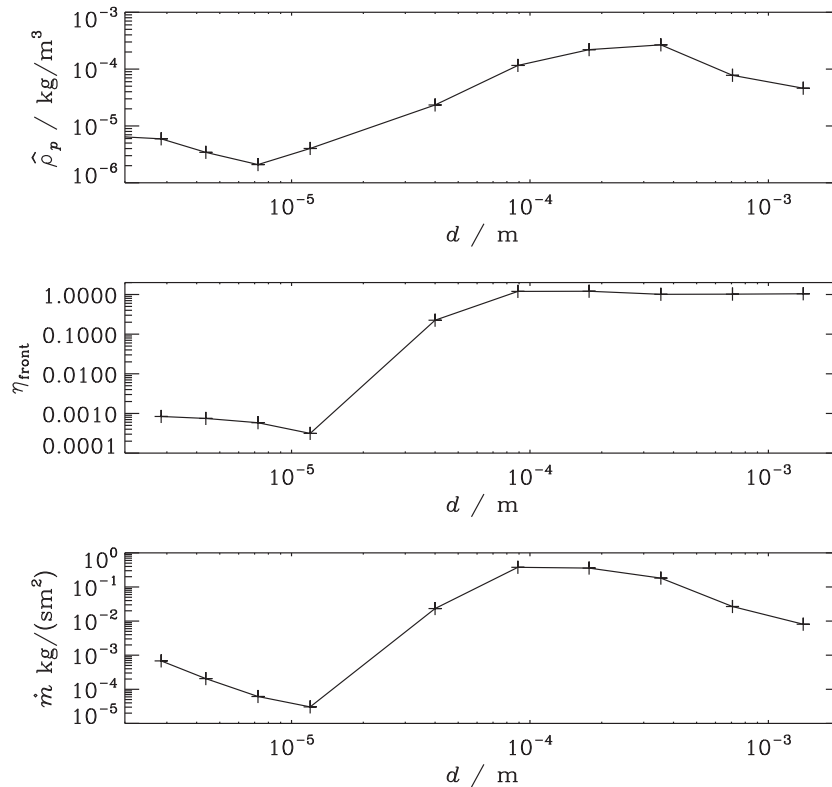
Fig. 5. The upper plot shows the mass density for different particle sizes, while the middle plot shows the total impaction efficiency. Finally the lower plot shows the specific rate of mass impaction on the front side of the tubes, per tube length, summed over all tubes in a tube row. The values result from a combination of simulation data and measurements from the MSWI in Schweinfurt, Germany.

4. Conclusion

In this work DNS has been used in order to accurately simulate particle impaction on a tube bundle. The tube bundle dimensions have been chosen according to the super heater in the MSWI in Schweinfurt, Germany. It is found that the particle impaction efficiency, both on the front and back side of the tubes, is very dependent on Reynolds number. This is in particular true for the front side capture of particles in the diameter range of 10–100 μm, where the difference between Re = 1685 and Re = 421 is of several orders of magnitude. It must be highlighted here, though, that only the drag force has been included. The inclusion of additional forces such as Brownian motions

and thermophoresis is expected to have a significant effect for small particle sizes. Allowing for the flow entering the super heater tube bundle to be turbulent may also have an effect on the results, as will the particle sticking coefficient which in this study is chosen to be one.

It is shown that the back side impaction efficiency is significantly increased for large Reynolds numbers. This is due to the increased intensity in the eddies generated by the tubes as the Reynolds number is increased.

Finally measurements of the particle size distribution found in the MSWI in Schweinfurt are presented. These measurements are then used to find quantitative results for the particle impaction rate due
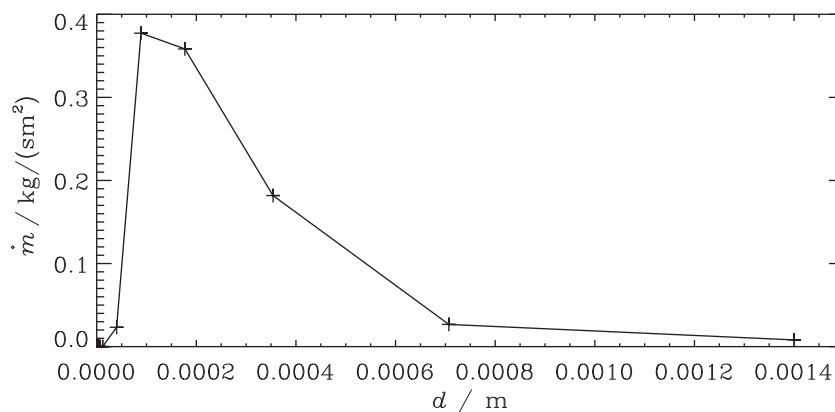

Fig. 6. The total specific rate of mass impaction on the front side of all the tubes in a tube row, per tube length.
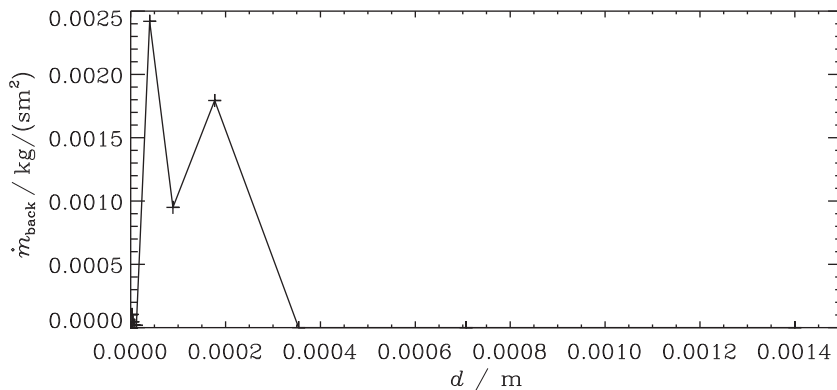
Fig. 7. The total specific rate of mass impaction on the back side of all the tubes in a tube row, per tube length.

to inertial impaction for different particle diameters. It is found that the largest part of the mass impaction is found for particles in the range from 5×10^{-5} m to 7×10^{-4} m.

Acknowledgements

References

[1] M. Jöller, T. Brunner, I. Obernberger, Fuel Processing Technology 88 (2007) 1136–1147.
[2] Z. Ma, F. Iman, P. Lu, R. Sears, L. Kong, A.S. Rokanuzzaman, D.P. McCollor, S.A. Benson, Fuel Processing Technology 88 (2007) 1035–1043.
[3] X. Li, H. Zhou, K. Cen, Fuel 87 (2008) 1379–1382.
[4] L.Y. Huang, J.S. Norman, M. Pourkashanian, A. Williams, Fuel 75 (1996) 271–279.
[5] D. Loehden, P.M. Walsh, A.N. Sayre, J.M. Beer, A.F. Sarofim, Journal of the Institute of Energy (1989) 119–127.
[6] S. Yilmaz, K.R. Cliffe, Journal of the Institute of Energy (2000) 65–68.
[7] H. Wu, P. Glarborg, F.J. Frandsen, K. Dam-Johansen, P.A. Jensen, Energy & Fuels 25 (2011) 2862–2873.
[8] S.K. Suneja, C.H. Lee, Atmospheric Environment 8 (1974) 1081–1094.
[9] E. Schweers, H. Umhauer, F. Löffler, Particle and Particle Systems Characterization (1994) 275–283.
[10] W. Muhr, Dissertation, Institut fürMechanische Verfahrestechnik und Mechansik, Universität Karlsruhe, 1976.
[11] G. Kasper, S. Schollmeier, J. Meyer, J. Hoferer, Journal of Aerosol Science 40 (2009) 993–1009.
[12] J.Y. Tu, C.A.J. Fletcher, Y.S. Morsi, W. Yang, M. Behnia, Chemical Engineering Science 53 (1998) 225–238.
[13] Y.S. Morsi, J.Y. Tu, G.H. Yeoh, W. Yang, Chemical Engineering Science 59 (2004) 3141–3157.
[14] Z. Tian, J. Tu, G. Yeoh, Computers and Chemical Engineering 31 (2007) 1064–1072.
[15] K. Sandström, C. Mueller, M. Hupa, Fuel Processing Technology 88 (2007) 1053–1060.
[16] R. Scharler, J.G.M. Kuerten, K. Schulze, I. Obernberger, Vdi berichte 1988 (2007) 299–312.
[17] N.E.L. Haugen, S. Kragset, Journal of Fluid Mechanics 661 (2010) 239–261.
[18] R. Kouznetsov, M. Sofiev, Journal of Geophysical Research 117 (2012) D01202.
[19] R. Weber, M. Mancini, N. Schaffel-Mancini, T. Kupkam, Fuel Processing Technology (2011), http://dx.doi.org/10.1016/j.fuproc.2011.09.008.
[20] GKS - Gemeinschaftskraftwerk Schweinfurt GmbH, http://www.gks-sw.de/ 2009.
[21] R. Warnecke, M. Weghaus, S. Horn, F. Haider, S. Maisch, V. Müller, H. Nordsieck, Entwicklung zur Beschreibung der Geschwindigkeit der Hoch-Temperatur-Chlor-Korrosions, in: VDI-Wissensforum (Ed.), Feuerung und Kessel - Beläge und Korrosion in Großfeuerungsanlagen, Düsseldorf, Germany, 2009.
[22] The pencil code, http://www.nordita.org/software/pencil-code 2009.
[23] C. Deuerling, J. Maguhn, H. Nordsieck, B. Benker, R. Zimmermann, R. Warnecke, Heat Transfer Engineering 30 (2009) 822–831.